The Proton and Occam's Razor

Giorgio Vassallo[1], **Andras Kovacs**[2]

[1]Università degli Studi di Palermo (Dipartimento di Ingegneria), Palermo, Italy

[2]BroadBit Energy Technologies, Espoo, Finland

E-mail: giorgio.vassallo@unipa.it

Abstract. Otto Stern's 1933 measurement of the unexpectedly large proton magnetic moment indicated to most physicists that the proton is not a point particle. At that time, many physicists modeled elementary particles as point particles, and therefore Stern's discovery initiated the speculation that the proton might be a composite particle. In this work, we show that despite being an elementary particle, the proton is an extended particle. Our work is motivated by the experimental data, which we review in section 1.

By applying Occam's Razor principle, we identify a simple proton structure that explains the origin of its principal parameters. Our model uses only relativistic and electromagnetic concepts, highlighting the primary role of the electromagnetic potentials and of the magnetic flux quantum $\Phi_M = {}^{h}/_{e}$. Unlike prior proton models, our methodology does not violate Maxwell's equation, Noether's theorem, or the Pauli exclusion principle.

Considering that the proton has an anapole (toroidal) magnetic moment, we propose that the proton is a spherical shaped charge that moves at the speed of light along a path that encloses a toroidal volume. A magnetic flux quantum $\Phi_M = {}^{h}/_{e}$ stabilizes the proton's charge trajectory. The two curvatures of the toroidal and poloidal current loops are determined by the magnetic forces associated with Φ_M. We compare our calculations against experimental data.

keywords
Aharonov-Bohm electrodynamics, magnetic flux quanta, nuclear anapole moment, Occam's razor, proton model, unified field theory, vector potential, Zitterbewegung.

1. Motivation

1.1. A brief history of the proton model

Before the 1970s, most scientists viewed the proton as an elementary particle. Starting from the 1970s, scientists working with high energy particle colliders proposed that protons and neutrons are not elementary particles, but comprise smaller sub-particles. According to their model, a proton and a neutron both comprise three quark sub-particles. The existence of quarks has been suggested initially in the 1960s, based on the theoretical efforts by Gell-Mann to model baryons and mesons [13], which were observed in a great variety during high energy nuclear experiments. The momentum distribution of particles emerging from a high-energy collision is characterized by the F_2 structure function[1]. Feynman's proposition was that the F_2 structure

[1] A detailed explanation of the $F_1(x)$ and $F_2(x)$ structure functions can be found for example in [24]. In these functions, the variable x measures the fraction of the nucleon's longitudinal momentum carried by the struck

function probes the internal momentum distribution of sub-particles; for a particle comprising N sub-particles, its F_2 structure function must peak at $x = \frac{1}{N}$. Gell-Mann's original quark theory thus required the F_2 momentum distribution to peak at $x = \frac{1}{3}$. However, as will be shown in section 1.3, this is not the case because the experimentally observed F_2 data peaks at $x = \frac{1}{9}$. This deviation from the required peak at $x = \frac{1}{3}$ was explained away via the hypothesis that the three quarks originally thought to form the proton are the so-called "valence quarks", which are swimming in the background of "sea quarks" [6]. These so-called sea quarks are a collection of quark-antiquark pairs, radiated by the three valence quarks. However, the calculations of 1970s still showed that the valence quarks together with the sea quarks only accounted for 54% of the proton's momentum [16]. A further hypothesis was added to supplement the momentum shortfall of the quarks; chargeless particles called gluons were introduced into the proton model [25]. Since gluons have no electric charge, the thinking was that they are there, but the electrons probing the proton in deep inelastic scattering cannot see them. These hypothesized gluons were assigned the missing proton momentum, and the resulting proton model became the quark-gluon model that it is today. Despite the absence of any direct quark observation, the quark-gluon model gained popularity during the 1970s, and remained embraced by most theoretical physicists ever since.

According to the 1970s model of "valence quarks" swimming in the background of "sea quarks and gluons", there seemed to be an angular momentum deficit with respect to the measured angular momentum of the proton, and therefore the presence of "virtual strange quarks" was also postulated during the 1990s [20].

In the context of quark theory, the fulfillment of $F_2(x) = 2xF_1(x)$ relation around $x = \frac{1}{3}$ means that an individual quark's spin is detectable[2]. Since the proton's magnetic moment measurements yield a constant value of $\mu_p = 2.793\mu_N$, quark proponents postulated that the three valence quarks are always spin correlated and that the sea quarks' spin contribution always sums up to zero. The $\mu_p \approx 3\mu_N$ relation has been interpreted as the almost parallel orientation of the three valence quark spins. It was pointed out to pioneering quark proponents that their requirement is in contradiction with the Pauli exclusion principle. This issue lead Oscar Greenberg to postulate in 1964 that quarks also have "color charge"; the purpose of this color charge hypothesis was to remove the contradiction with respect to the Pauli exclusion principle.

1.2. Experimental counter-evidence to the quark model

Although the quark-based model was inspired by the great variety of mesons, the proposed quark masses do not add up the masses of observed mesons. According to quark proponents, this is explained by a negative binding energy between quarks: any particle's valence quarks masses are only a small percentage of the total particle mass, with the bulk of the particle mass coming from virtual particles which represent the binding force: i.e. virtual quarks and gluons. Moreover, the valence quark : virtual quark : gluon mass ratio is allowed to vary from particle to particle in order to match the observed masses. Now what is the physical meaning of negative binding energy? By definition, negative binding energy means a metastable bound state. This model implies that individual quarks should be easily observable upon the break-up of their metastable binding. However, quark proponents also postulated that these metastable bonds between quarks can never be dissociated. There is a fundamental contradiction between the hypothesis of metastable quark binding and the hypothesis of unbreakable quark bonds.

particle, evaluated in the Breit frame. The $F_1(x)$ function at a given x is interpreted as $\frac{1}{2}$ of the likelihood of scattering from a particle which, in the Breit frame, has longitudinal momentum fraction x of the proton. In case of scattering from spin-$\frac{1}{2}$ particles, $F_2(x) = 2xF_1(x)$.

[2] The $F_2(x) = 2xF_1(x)$ equation is referred to as the Callan-Gross relation. Scattering experiments have indeed observed this Callan-Gross relation, at least within the $x = [0.25, 0.75]$ range.

Proton-antiproton reactions provide rather direct counter-evidence. Figure 1.1 shows traces of a proton-antiproton reaction event, highlighting the produced pion tracks. According to the quark model, a proton-antiproton pair comprises six quarks. After a partial annihilation of quark-antiquark pairs, there can be up to four remaining quarks, which may be organized into two pions. However, figure 1.1 shows at least eight pions emerging from the annihilation event, which contradicts the quark model. A quark model proponent may try to explain this phenomenon by assuming that the kinetic energy of the incoming antiproton was converted into the production of numerous pion-antipion pairs just prior to its annihilation. However, such an explanation is refuted by reference [7], whose authors exposed a nuclear emulsion to antiprotons, and then analyzed the resulting tracks in the emulsion. Their discussion of figure 2 in reference [7] clearly states that the antiproton first came to a rest in the emulsion, and then produced at least five pions upon annihilation with a proton. Such large number of pions emerging from proton-antiproton reactions is impossible under the quark-antiquark annihilation model.

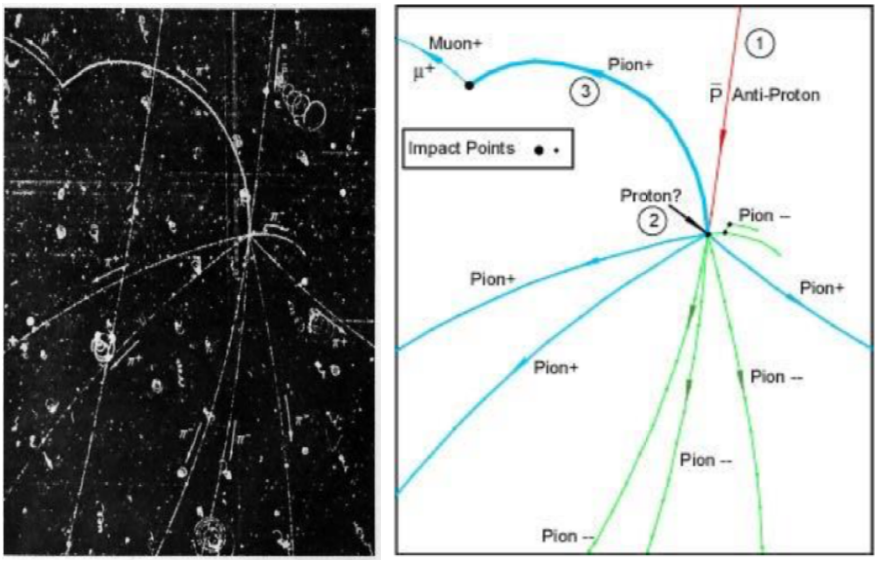

Figure 1.1. Proton-antiproton annihilation event. Left: bubble chamber photograph. Right: diagram of the photo, identifying the particles created by the annihilation event. Source: Lawrence Berkeley National Laboratory Science Photo Library - photograph K003/4377.

According to the quark model, the proton and neutron both comprise three quarks, only differing in one quark type. However, a recent work [23] establishes that the neutron comprises a positive and a negative elementary charge, which again invalidates the quark-gluon model.

Finally, we mention that the postulated spin correlation among the three valence quarks leads to a mathematical paradox, that will be discussed in section 6.

1.3. A re-interpretation of high-energy particle collision data

Considering the above outlined problems with the quark-based proton model, one may wonder about the origin of the F_2 momentum-distribution data recorded in high-energy collisions.

The production of particle-antiparticle pairs is a well established phenomenon of high-energy collisions. Therefore, an incoming energetic electron may produce muon-antimuon pairs upon scattering. Also, an incoming electron may be energized into a muon upon scattering. It is thus pertinent to consider a relationship between the F_2 data and the short-lived particles produced in preceding scattering events.

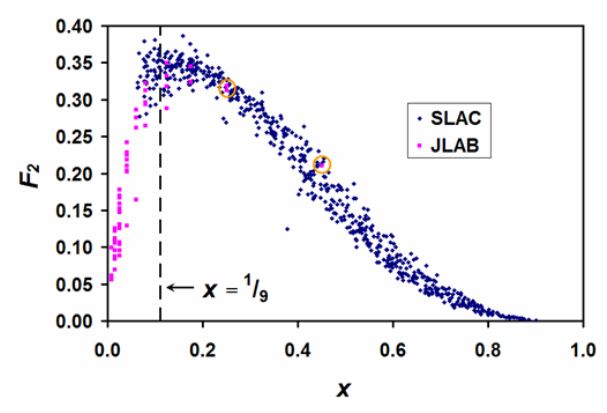

Figure 1.2. Combined SLAC and JLAB data of F_2 momentum distribution measurements from electron-proton scattering, reproduced from [37].

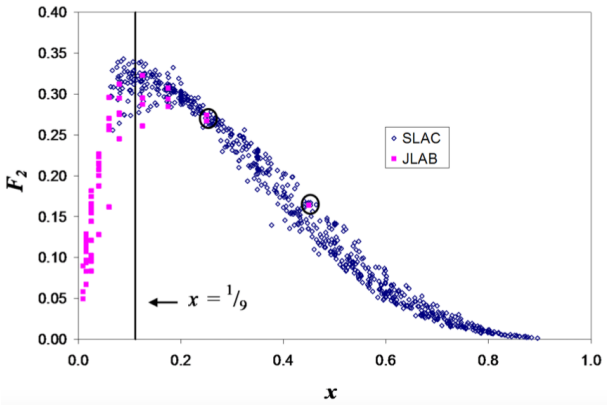

Figure 1.3. Combined SLAC and JLAB data of F_2 momentum distribution measurements from electron-deuteron scattering, reproduced from [37]. This scattering data shows the same F_2 momentum distribution as in the electron-proton case.

Reference [37] presents a thorough analysis of high energy scattering data from measurements performed at the Stanford Linear Accelerator Center (SLAC), Thomas Jefferson National Accelerator Facility (JLAB), and Hadron Electron Ring Accelerator (HERA). As shown in figures 1.2 and 1.3, the combined SLAC and JLAB data of F_2 momentum distribution measurements shows clearly, without any curve fittings, that their F_2 values peak in the vicinity of $x = \frac{1}{9}$. The JLAB F_2 values at $x = 0.45$ and $x = 0.25$ (circled) show that JLAB data integrates well with the original SLAC F_2 data. Is the use of single-variable $F_2(x)$ distribution justified, i.e. are the energy and momentum exchange sufficiently high for convergence? The use of $F_2(x)$ rather than $F_2(x, Q^2)$ is justified because the SLAC data was shown to satisfy Bjorken scaling, i.e. for x>0.2, the F_2 values are essentially the same for a given x regardless of the Q amount of energy transferred between the scattering particles. In this x>0.2 region, Q^2 values range from 0.6 to about 30 GeV^2. Regarding the x<0.2 region, the JLAB Q^2 values shown in Figure 1.4 are nearly the same as the SLAC Q^2 values listed in Appendix A.1 of [37], which makes the two results directly comparable.

One may wonder why this F_2 peak at $x = \frac{1}{9}$ doesn't show up in any other literature? By 1973, mainstream theorists have essentially embraced the quark-gluon model as adequately describing the structure of the proton. Most attempts to explain the SLAC scattering results any other

x	Q^2	F_2 - p	F_2 - d	x	Q^2	F_2 - p	F_2 - d
0.009	0.034	0.056	0.0492	0.04	0.287	0.2027	0.2002
0.009	0.051	0.0616	0.058	0.04	0.353	0.2244	0.2077
0.009	0.086	0.0997	0.0896	0.04	0.37	0.2288	0.2139
0.015	0.059	0.0696	0.0669	0.04	0.371	0.2186	0.2155
0.015	0.095	0.0842	0.0831	0.04	0.38	0.2102	0.2231
0.015	0.098	0.0961	0.0935	0.04	0.421	0.2416	0.2268
0.015	0.112	0.0876	0.0966	0.06	0.18	0.1641	0.1616
0.015	0.127	0.1058	0.1073	0.06	0.479	0.2622	0.2563
0.015	0.144	0.1114	0.1129	0.06	0.491	0.2617	0.2702
0.015	0.151	0.1216	0.1186	0.06	0.543	0.2751	0.2609
0.015	0.164	0.1253	0.1227	0.06	0.633	0.2863	0.2958
0.015	0.172	0.1118	0.1286	0.08	0.456	0.265	0.2451
0.025	0.067	0.0883	0.0834	0.08	0.617	0.2935	0.2752
0.025	0.092	0.096	0.0953	0.08	0.619	0.296	0.2767
0.025	0.104	0.104	0.0994	0.08	0.799	0.3128	0.295
0.025	0.113	0.1069	0.1024	0.08	0.818	0.3227	0.3122
0.025	0.14	0.1251	0.1208	0.125	0.588	0.2876	0.2609
0.025	0.186	0.1469	0.1441	0.125	0.797	0.3179	0.2873
0.025	0.195	0.1312	0.1439	0.125	1.032	0.3319	0.2952
0.025	0.212	0.1675	0.1545	0.125	1.056	0.3491	0.3228
0.025	0.222	0.1593	0.1568	0.175	1.029	0.3242	0.2846
0.025	0.24	0.178	0.1656	0.175	1.045	0.3235	0.2939
0.025	0.252	0.1696	0.1745	0.175	1.365	0.3447	0.3072
0.025	0.253	0.153	0.1601	0.25	1.332	0.3126	0.2673
0.025	0.287	0.1669	0.1814	0.25	1.761	0.3183	0.2744
0.04	0.133	0.1295	0.128	0.45	2.275	0.2104	0.1638
0.04	0.273	0.2038	0.1876				

Figure 1.4. F_2 structure function values for the proton (F_2 - p) and the deuteron (F_2 - d) as a function of x and Q^2 from the JLAB E99-118 deep inelastic scattering experiments [38].

way had ended, and the bulk of the theoretical effort focused on enhancing the quark model. Different versions of the quark-gluon plasma model predict either constant or rising F_2 values as $x \to 0$. In the 1990s, when HERA experiments began producing data in this $x<0.1$ range, it was assumed that HERA filled the low-x gap left by SLAC, even though its data was generated from scatterings with Q^2 values tens to hundreds of times higher than the SLAC data. Many theorists could not resist the temptation of mixing non-comparable data in this low-x region of the F_2 curve, and mistakenly proclaimed experimental support for their quark-gluon model. Reference [32] is a typical example of such erroneous data analysis. Around 2000, the JLAB experiment began producing scatterings with comparable Q^2 values to the SLAC experiment. By that time, the erroneous blending of high-Q^2 HERA data with low-Q^2 SLAC data was already a consensus procedure for obtaining the proton's F_2 curve, and mainstream theorists had no interest in pointing out their colleagues' mistakes or discussing the implications of the JLAB experiment.

Upon dividing the proton's mass by 9, we obtain approximately the muon mass. This match with the F_2 peak location at $x = \frac{1}{9}$ suggests that it may correspond to electron scattering from a muon or antimuon that was produced in some preceding scattering event. Our interpretation implies that one should also find a peak corresponding to electron-electron scattering in the very low-x region because an incoming electron may also collide with a previously scattered other electron. Upon the analysis of HERA experiments, reference [37] indeed identifies yet another F_2 momentum distribution peak near $x = \frac{1}{1836}$, which corresponds to the electron mass.

Since there is no F_2 peak at $x = \frac{1}{3}$, the fulfillment of Callan-Gross relation around $x = \frac{1}{3}$ simply means that the energetic electron is mainly scattering from the proton, which is a spin-$\frac{1}{2}$ particle.

In summary, the F_2 momentum distribution data shows signatures of electron-muon and electron-electron scattering. Consequently, the quark model is contradicted by all experimental data. The absence of a reasonable proton model motivates us to explore the proton's internal structure.

Antiprotons are generated in sufficiently energetic collisions between light and heavy nuclei. Would a violent collision create complex structures involving many sub-particles? That would be very unlikely, and it is moreover favored by Occam's razor principle to firstly explore simple

proton structures. We thus investigate whether a relatively simple proton model exists, which would match its experimentally observed properties.

2. How large is the proton?

2.1. The proton's spherical charge radius

Any particle's Compton scattering cross-section is given by the Klein-Nishina formula, where one parameter is the spherical charge radius. Upon fitting the electron's experimental Compton scattering cross-section to the Klein-Nishina formula, in the 0.5 MeV photon energy range, one obtains 2.82 fm spherical charge radius. This 2.82 fm electron charge radius is referred to as the classical electron radius in the scientific literature.

Is the same method applicable for determining the proton's spherical charge radius? Figure 2.1 shows the proton's scattering cross-section in the 1 GeV photon energy range, which corresponds to the proton mass. There are numerous peaks in the scattering data of figure 2.1; these correspond to photo-production of new particles. Experimental measurements determined that the largest peak around 300 MeV corresponds to the photo-production of two neutral pions, while the peak around 700 MeV corresponds to the photo-production of a pion and an η meson. In contrast to the electron case, the scattering cross-section is now a sum of particle photo-production and Compton scattering processes. Nevertheless, we can make an estimation of the proton's spherical charge radius.

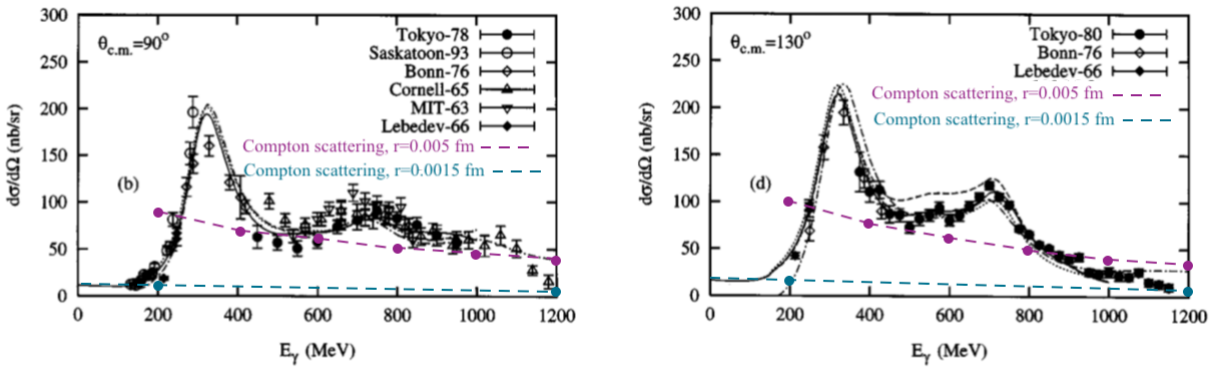

Figure 2.1. The proton's interaction cross-section with high frequency radiation, reproduced from [28]. The horizontal scale shows the incoming photon energy, the left and right panels show the cross-section at 90° and 130° scattering angles, respectively. The red and and blue dashed lines show the Compton scattering cross-section for the indicated spherical charge radius values.

The dashed lines on figure 2.1 show the Compton scattering cross-section at $5 \cdot 10^{-18}$ m and at $1.5 \cdot 10^{-18}$ m spherical charge radius values. With $5 \cdot 10^{-18}$ m radius, the Compton scattering cross-section becomes larger than the experimental values in the $<$200 MeV and $>$1000 MeV regions. Therefore, the true radius is smaller than $5 \cdot 10^{-18}$ m. In contrast, with $1.5 \cdot 10^{-18}$ m radius value the Compton scattering cross-section converges to the experimental values both in the $<$200 MeV and $>$1000 MeV regions. Therefore, light scattering measurements indicate that the proton's spherical charge radius is approximately $1.5 \cdot 10^{-18}$ m.

2.2. The proton's apparent Zitterbewegung radius

Numerous experiments aim to precisely measure the proton's so-called "charge radius", which is defined as the mean radius value of its charge distribution. High-energy electron-proton scattering experiments are one class of such measurements.

As shown in table 1, one of the earliest scattering analysis based proton charge radius extraction was published in 1963: it comprises a systematic review of scattering experiments performed up to that date, and its authors calculated a $0.805 \cdot 10^{-15}$ m charge radius value. By the early 2000s, the consensus mean proton radius value increased to $0.875 \cdot 10^{-15}$ m, but reference [27] re-analyzes the involved measurements and claims to have found a systemic error which caused over-estimations.

Recent measurements converge around the $0.84 \cdot 10^{-15}$ m mean radius value, and claim very small error margins of only $(5-8) \cdot 10^{-18}$ m.

This $0.84 \cdot 10^{-15}$ m mean radius value is several orders of magnitude larger than the above identified $r_{cp} < 5 \cdot 10^{-18}$ m parameter. To understand the physical meaning of the $0.84 \cdot 10^{-15}$ m radius value, we again use the analogy of electron scattering experiments. When an electron interacts with high frequency light, its scattering cross section is given by the Klein-Nishina formula, and such scattering data reveals the electron's 2.82 fm spherical charge radius. When an electron interacts with low frequency light, its scattering cross section is given by the Thomson scattering formula, and such scattering data reveals the electron's 386 fm Zitterbewegung radius. In the scientific literature this electron Zitterbewegung radius is also referred to as the electron's "reduced Compton radius". By analogy, we associate the proton's $0.84 \cdot 10^{-15}$ m radius value as an approximation of the major radius of the torus enclosed by the proton charge trajectory.

Publication year	Mean proton radius value	Reference
1963	0.805 ± 0.011 fm	[17]
2016	0.840 ± 0.016 fm	[14]
2020	0.831 ± 0.019 fm	[42]
2021	0.847 ± 0.008 fm	[10]
2022	0.840 ± 0.005 fm	[27]

Table 1. Electron-proton scattering analysis based mean proton radius measurements.

Besides the electron-proton scattering analysis, there are also spectroscopic methods for the proton's charge radius calculation [15]; all spectroscopic estimate the impact of non-zero proton radius on the electrostatic potential of the electron's wavefunction. Table 2 shows the results of recent proton radius measurements, based on spectroscopic methods.

Publication year	Involved particles	Charge radius	Reference
2017	e^-, p^+	0.8335 ± 0.0095 fm	[4]
2019	e^-, p^+	0.833 ± 0.01 fm	[5]
2020	e^-, p^+	0.8483 ± 0.0038 fm	[15]

Table 2. Spectroscopic analysis based mean proton radius measurements.

Tables 1 and 2 show remarkably similar values. Omitting the 1963 data, the remaining recent measurements average out to $r_{mean} = 0.839 \pm 0.007$ fm.

2.3. Charge density measurements

With the advancement of electron-proton scattering measurements, it has become possible to directly map out the proton's radial charge distribution. Such radial charge distribution data is measured for example at JLAB [8], and is visualized in figure 2.2. This distribution's average RMS (Root Mean Square) value is 0.8 fm, which implies only 4% deviation from the data of

tables 1 and 2. Figure 2.2 conveys the important information that the proton charge is located mainly within 0.2-1 fm from its center. Any realistic proton model must yield a similar radial distribution range.

One can also calculate the radius within which 50% of the proton charge is contained. As can be seen in figure 2.2, the radius value at the 50% cumulative charge is $r_{phc} \simeq 0.627$ fm. Here, the "phc" index refers to the proton half-charge radius. An interpretation of this experimental value will be addressed in section 5.5.

The r_{mean} and r_{phc} values are two distinct measures of the proton size. The relevant measure to use depends on the context.

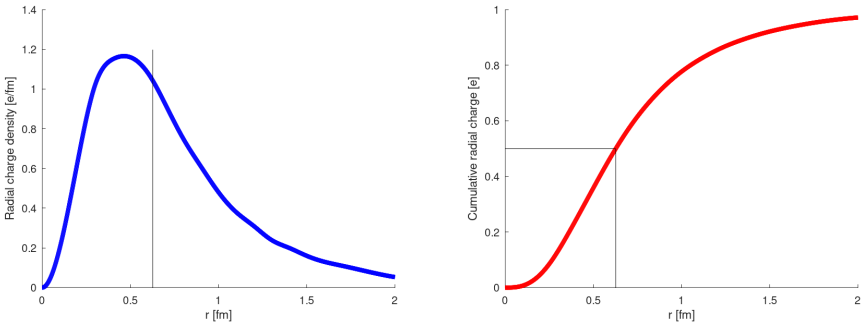

Figure 2.2. The proton's radial charge distribution, according to JLAB measurements [8]. Left: the proton's radial charge density. Right: the cumulative proton charge contained within a given radius. In both charts, the black vertical line indicates the radius $r_{phc} \simeq 0.627$ fm which contains 50% of the total charge.

2.4. The proton's electric polarizability radius

Electric polarizability measurements represent yet another proton size measurement method. Recent measurements by this method are reported in references [26, 12]: their authors obtain $1.2-1.3$ fm proton size. This size is significantly larger than the above-mentioned Zitterbewegung radius measurements, and the origin of such discrepancy has not been understood in preceding works.

3. Methodology

In this work, we explore an electromagnetic proton structure which is in accordance with Maxwell's equation. Our methodology is based on the recently published electron model [22], which explains what an electron is made of, why it has a spin, and what the origin of the quantum mechanical wavefunction is. A main conclusion of [22] is that the electron mass comprises electromagnetic field energy. Given that a high-frequency electromagnetic wave can produce an electron-positron pair, while traveling through a sufficiently strong electric field, the ideas of [22] are quite natural. More specifically, by calculating the electric field energy around the electron's 2.82 fm spherical charge radius, one obtains 255.5 keV, which is exactly half of the electron mass. As explained in [22], the other half of the electron mass is magnetic field energy. These two electromagnetic energy types continuously induce each other. Such dynamics is completely analogous to the perpetual induction within an electromagnetic wave, which may give birth to the electron-positron pair.

The 255.5 keV magnetic energy of an electron corresponds to the circular Zitterbewegung of its spherical charge. Such circular Zitterbewegung generates the electron spin. The constant value of the electron spin follows from the constant speed of its circular Zitterbewegung; as discussed

in [22], it directly follows from gaugeless Maxwell's equation that the Zitterbewegung speed is the speed of light.

As outlined in table 3, our methodology is in accordance with all fundamental physical laws. In comparison, the quark-based methodology has multiple drawbacks: i) the quark model violates foundational laws, such as Maxwell's equation or Noether's theorem, ii) as explained in section 1, the quark model lacks any experimental evidence, and iii) the quark model is contradicted by the commercial Nuclear Magnetic Resonance (NMR) technology. The implications of proton NMR data will be discussed in section 6.

	Quark-based proton model	**This work**
Violates Maxwell's equation?	Yes (point-like charges)	No
Neglects infinite quantities?	Yes (renormalization)	No
Violates Noether's theorem?	Yes (virtual particles)[3]	No
Relation to NMR measurements?	Contradicts p^+ NMR data	Explains p^+ NMR
Radius calculations can be verified?	No (too lengthy/complex)	Yes

Table 3. A comparison between the quark-based proton model and our present work.

At first it seems natural to use the exact same model for describing both the electron and proton, scaling the given particle's dimensions by the appropriate particle mass. The advantages of a simple ring-shaped proton model were indeed pointed out by David L. Bergman in his paper "The Real Proton" [2]. This approach, while works well for muons, introduces unacceptably large errors if naively used for proton modeling. Firstly, the magnetic moment of such a simple model is equal to the nuclear magneton μ_N, while the experimental proton magnetic moment value is approximately 2.79 times larger. Secondly, as discussed in section 2.2, the proton's experimental Zitterbewegung radius value is 0.839 ± 0.007 fm, while the "scaled positron" model yields a 0.2103 fm Zitterbewegung radius from the $e^+ : p^+$ mass ratio. The following sections present a simple proton model that overcomes these large discrepancies while fully maintaining the conceptual framework introduced in this section.

4. Gaugeless electrodynamics

It's important to note that, at the Compton scale, certain quantized physical values appear dimensionless in natural units. The elementary charge value $e = \pm\sqrt{\alpha}$, its magnetic flux $\Phi_M = {}^{2\pi}/_{e}$, Zitterbewegung speed $c = 1$, and angular momentum $\hbar = 1$ *cannot be separated but are different characteristics of the same physical entity.* As already pointed out in [22, 11], a non-linear dynamic equation can be derived when the Maxwell's equation and the Proca equation are considered to apply simultaneously. This equation essentially describes, using the language of spacetime Clifford Algebra $Cl_{3,1}(\mathbb{R})$, the behavior of an elementary charge that always moves at the speed of light and is subjected to a magnetic centripetal force that is responsible for the curvatures of its Zitterbewegung trajectory. Therefore, the electromagnetic four-potential can be seen as the field, a "*Materia Prima*", from which the physical entities that we call "particles" are generated. It is therefore reasonable to universally apply this approach to all charged elementary particles.

Leaving behind the experimentally paradoxical hypothesis of electromagnetic gauges [36, 9, 35], we do not assume the presence of any electromagnetic gauge, and arrive at the simplest form of Maxwell's equation [22, 11, 3]: $\boldsymbol{\partial}^2 \boldsymbol{A}_{\square} = 0$. The $\boldsymbol{A}_{\square}$ notation refers to the electromagnetic four-potential $\boldsymbol{A}_{\square} = \boldsymbol{A} + \gamma_t V$. The electric charges and currents then correspond to a scalar field on a spherical surface. As required by Maxwell's equation, this charged surface

[3] The quark-based model assigns over 98% of the proton mass to virtual particles.

is moving at light speed, and is characterized by a vector potential $\boldsymbol{A}$, an electric potential V, a current $I = {}^{\alpha A}/_{2\pi}$, a mechanical momentum $m\boldsymbol{c} = e\boldsymbol{A}$, and an angular speed $\omega = eA$. Respecting both magnetic and electric Aharonov-Bohm relations, the charge's electromagnetic four potential $\boldsymbol{A}_{\square} = \boldsymbol{A} + \gamma_t V$ is a nilpotent vector $\left(\boldsymbol{A}_{\square}^2 = 0\right)$. These laws may be considered as a powerful tool for modeling the structure and properties of elementary charged particles. Prior to [22, 11], gaugeless electrodynamics has been already introduced and explored by other authors [1, 18, 19, 21, 29, 30, 31, 33, 34, 39, 41]. Most of these preceding works introduce the electromagnetic scalar field as an additional entity besides charges and currents, rather than the entity that actually produces the apparent charges and currents. A notable exception is the work of Giuliano Bettini [3] that recognizes the electromagnetic sources as the partial derivatives of the scalar field.

The elementary charge is characterized by a simple Lagrangian $\mathscr{L}$ that defines the action $\mathscr{S}$:

$$\mathscr{L} = e\boldsymbol{A} \cdot \boldsymbol{c} - eV \tag{4.1}$$

$$\mathscr{S} = \int \mathscr{L} dt$$

The stationary action condition $\delta\mathscr{S} = 0$ is a consequence of the Aharonov-Bohm relations

$$\mathscr{S} = \int \left(e\boldsymbol{A} \cdot \boldsymbol{c} - eV\right) dt = e \int \boldsymbol{A} \cdot \boldsymbol{dl} - e \int V dt = 0$$

$$\delta\mathscr{S} = 0$$

As $\boldsymbol{A}$ and $\boldsymbol{c}$ are parallel vectors for a freely moving charge, it's possible to substitute the dot product with the product of their modulus:

$$\mathscr{L} = eAc - eV = eA\frac{dl}{dt} - eV$$

If the radius of the charge's Zitterbewegung trajectory is r, the differential of the displacement dl can be substituted by the product $rd\varphi$:

$$dl = rd\varphi$$

$$\mathscr{L} = eAr\frac{d\varphi}{dt} - eV$$

Consequently, the following simple conditions guarantee that the action $\mathscr{S}$ is always zero:

$$eAr = \hbar = 1$$

$$\frac{d\varphi}{dt} = eV = eA = \frac{1}{r}$$

$$r^{-1} = \frac{d\varphi}{dt} = \omega = m$$

In natural units, the elementary particle's mass-energy is equal to its Zitterbewegung angular speed, to the inverse of its Zitterbewegung radius, and to the value its Zitterbewegung momentum eA.

5. Proton model

5.1. Proton geometric structure

We develop our proton model in agreement with the above considerations. While the natural choice for a proton model is a simple "scaled positron" model, it leads to some unacceptable discrepancies with the experimental data, that we have already pointed out.

Measurements of the proton's anapole magnetic moment have been claimed since 1997 [40]. In such experiments, electron-proton coupling interactions are used for mapping out the proton's various magnetic modes. Since the anapole magnetic moment is generated by a toroidal charge current, these experiments suggest that the proton's charge moves on a toroidal surface.

We therefore consider a model where the stationary proton charge follows a toroidal Zitterbewegung trajectory, similar to a toroidal coil winding. The toroidal volume enclosed by the proton charge trajectory has a minor (poloidal) proton radius r_{pp}, which remains to be determined.

At the Compton radius scale, the magnetic flux quantum $\hbar/e$ induces a centripetal magnetic force that constrains an elementary particle to follow either a circular Zitterbewegung path (positron case) or helicoidal Zitterbewegung path (proton case).

In this article, we describe two ways of applying our methodology to a toroidal proton model. These two approaches agree on the spherical charge radius value, but yield slightly different toroidal charge radius values. One approach, which represents the perspective of one author, is described in sections 5.2-5.5 of this article[4]. This first approach yields a toroidal charge radius that coincides with the measured r_{50c}=0.624 fm value. The other approach, which represents the perspective of the other author, is described in the first appendix. This second approach yields a toroidal charge radius that coincides with the measured $r_{mean} = 0.839$ fm value. We invite readers to analyze these two approaches, and debate the pros and cons for each one.

5.2. The proton's electromagnetic energy and charge radius

The proton charge is assumed to follows a closed helicoidal trajectory similar to a toroidal coil winding. The main geometric parameters of this model, such as its spherical charge radius or its toroidal and poloidal radii, can be found by starting from the proton mass-energy value and imposing the quantization of the angular momentum and of the experimental magnetic moment value.

The electric energy W_{pE} of the proton is calculated by integrating the energy density of its electric field down to its spherical charge radius r_{cp}:

$$W_{pE} = \frac{e^2}{8\pi}\int_{r_{cp}}^{\infty}\frac{1}{r^4}\cdot 4\pi r^2 dr = \frac{e^2}{2}\int_{r_{cp}}^{\infty}\frac{1}{r^2}dr = -\frac{e^2}{2}\frac{1}{r}\Big|_{r_{cp}}^{\infty} = \frac{e^2}{2r_{cp}} = \frac{\alpha}{2r_{cp}}$$

We assume that the electric energy is equal to one half of the proton mass, as required by Maxwell's equation for any electromagnetic wave. Introducing r_{pp} as the reduced Compton wavelength of the proton,

$$W_{pE} = \frac{m_p}{2} = \frac{1}{2r_{pp}}$$

and we calculate $r_{pp} = m_p^{-1} = 1.06578893\cdot 10^{-9}\, eV^{-1}\left(0.2103089103\cdot 10^{-15} m\right)$, as well as the proton charge radius:

$$\frac{\alpha}{2r_{cp}} = \frac{1}{2r_{pp}}$$

[4] This approach is the perspective of Giorgio Vassallo

$$r_{cp} = \alpha r_{pp}$$

$$r_{cp} = \frac{\alpha}{m_p} \simeq 7.777437549 \cdot 10^{-12}\, eV^{-1} \left(1.534698267 \cdot 10^{-18} m\right)$$

The other half of the proton mass comprises its magnetic energy W_{pM}:

$$W_{pM} = \frac{1}{2}\Phi_M I_p = \frac{1}{2} \cdot \frac{2\pi}{e} \cdot \frac{\alpha}{2\pi} A_p = \frac{1}{2} e A_p = \frac{m_p}{2}$$

The charge radius r_{cp} implies a potential V_p at the surface of the charge. Consequently it is in agreement with the electric Aharonov-Bohm 5.1equation if we assume that the charge spans an angle $d\varphi$ in a time dt moving at light speed $c = 1$:

$$d\varphi = \frac{cdt}{r_{pp}} = \frac{dt}{r_{pp}}$$

$$V_p = \frac{e}{r_{cp}}$$

$$d\varphi = eV_p dt \tag{5.1}$$

$$\frac{d\varphi}{dt} = eV_p = \frac{e^2}{r_{cp}} = \frac{\alpha}{r_{cp}} = \frac{1}{r_{pp}} = m_p$$

5.3. Proton torus aspect ratio

Assuming that the torus volume enclosed by the proton charge trajectory has a minor radius r_{pp} equal to the proton reduced Compton wavelength $\lambda_p/2\pi$ and that, using natural units, is equal to the inverse of the proton mass [2], it's possible to find the major radius imposing the quantization of the proton angular momentum L_p and the experimental value of the magnetic moment μ_p

$$L_p = m_p v_{pt} r_{pt} = \hbar = 1$$

$$v_{pt} = \frac{r_{pp}}{r_{pt}}$$

Multiplying the toroidal component I_{pt} of the proton current by the enclosed area πr_{pt}^2 we get the proton magnetic moment:

$$I_{pt} = I_p v_{pt} = \frac{\alpha}{2\pi} A_p v_{pt} = \frac{\alpha}{2\pi} A_p \frac{r_{pp}}{r_{pt}}$$

$$I_{pt} \pi r_{pt}^2 = \mu_p$$

$$\frac{\alpha}{2\pi} A_p \frac{r_{pp}}{r_{pt}} \pi r_{pt}^2 = \mu_p$$

remembering that $\alpha = e^2$ and that $eA_p = m_p = r_{pp}^{-1}$, we can write

$$\frac{e}{2} r_{pt} = \mu_p$$

$$r_{pt} = \frac{2\mu_p}{e} = 2.976586476 \cdot 10^{-9}\, eV^{-1} \left(0.5873608214 \cdot 10^{-15} m\right)$$

$$\mu_N = \frac{e}{2m_p}$$

$$\frac{r_{pt}}{r_{pp}} = v_{pt}^{-1} = \frac{2\mu_p}{e} m_p = \frac{\mu_p}{\mu_N} = \sqrt{\frac{39}{5}}$$

This means that the torus aspect ratio $\eta = \sqrt{39/5}$ is a value that is equal to the ratio of proton's magnetic moment and the nuclear magneton μ_N.

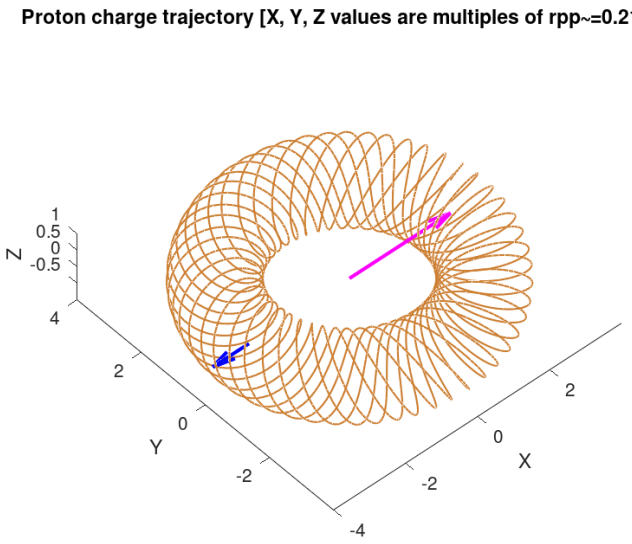

Figure 5.1. An illustration of the toroidal proton geometry. The brown curve is the Zitterbewegung trajectory, the blue arrow represents the poloidal proton radius (r_{pp}), and the purple arrow represents the toroidal proton radius (r_{pt}). The X, Y, Z values are multiples of $r_{pp} \simeq 0.21$ fm.

The toroidal component of a charge displacement equal to one Compton wavelength λ_p is equal to $\lambda_p v_{pt}$. The aspect ratio η implies that the proton charge travels along a path length of 39 λ_p after 5 turns around the torus center:

$$39\lambda_p v_{pt} = 5 \cdot 2\pi r_{pt}$$

$$39 \cdot 2\pi r_{pp} v_{pt} = 5 \cdot 2\pi r_{pt}$$

$$\frac{r_{pp}}{r_{pt}} v_{pt} = \frac{5}{39}$$

$$v_{pt} = \frac{r_{pp}}{r_{pt}}$$

$$v_{pt}^2 = \frac{5}{39}$$

$$v_{pt} = \eta^{-1} = \sqrt{\frac{5}{39}}$$

5.4. Proton charge and Lorentz force

The proton's charge has a mechanical momentum $m_p\boldsymbol{c}$ equal to the product of the elementary charge and its vector potential:

$$e\boldsymbol{A}_p = m_p\boldsymbol{c}$$

The proton charge is subjected to the magnetic Lorentz force:

$$\boldsymbol{F}_p = e\boldsymbol{c} \times \boldsymbol{B}_p = e\frac{d\boldsymbol{A}_p}{dt} = m_p\frac{d\boldsymbol{c}}{dt}$$

$$F_p = m_p\frac{c^2}{r_{pp}} = \frac{m_p}{r_{pp}} = r_{pp}^{-2}$$

The force vector $\boldsymbol{F}_p$ has a component F_{pt} that is always directed towards the torus' center

$$\boldsymbol{F}_{pt} = e\frac{d\boldsymbol{A}_{pt}}{dt} = eA_p\frac{d\boldsymbol{v}_{pt}}{dt} = m_p\frac{d\boldsymbol{v}_{pt}}{dt}$$

$$F_{pt} = m_p\frac{v_{pt}^2}{r_{pt}} = \frac{v_{pt}^2}{r_{pp}r_{pt}} = \frac{r_{pp}^2}{r_{pt}^3 r_{pp}} = \frac{r_{pp}}{r_{pt}^3}$$

The magnetic flux density $\boldsymbol{B}_p$ seen by the proton charge is one half the averaged valued of the magnetic flux density obtained dividing the magnetic flux $\Phi_M = {}^{2\pi}/_{e}$ by an area equivalent to the toroid cross section πr_{pp}^2

$$B_p = \frac{1}{2}\frac{\Phi_M}{\pi r_{pp}^2} = \frac{2\pi}{e\pi r_{pp}^2} = \frac{1}{er_{pp}^2}$$

5.5. The "proton charge radius" interpretation

Observing the proton on time scales much larger than the time required for a complete Zitterbewegung turn around the torus center, which is $T_{toroidal} = {}^{2\pi r_{pt}}/_{v_{pt}} \left(\simeq 3.44 \cdot 10^{-23} s\right)$, the charge appears confined inside a radius R_p equal to the sum of the two torus radii, r_{pt} and r_{pp}, and the proton's spherical charge radius $r_{cp} = \alpha r_{pp}$:

$$r_{pmax} = r_{pt} + r_{pp} + r_{cp} \simeq 0.7992 \cdot 10^{-15} m$$

.

Recent measurements of the "proton radius", which are listed in tables 1 - 2, average out to the following value: $r_{mean} \simeq (0.839 \pm 0.007) \cdot 10^{-15} m$. This value is 30% larger than the r_{pt} value calculated in sections 5.2-5.5.

Remembering however that r_{mean} is defined as the mean radius value of the charge distribution, this value, for the toroidal model, should be computed by the Root Mean Square distance r_{prms} of the charge from the toroid center in a time $T \gg \frac{2\pi}{\omega_{pt}}$ and a path length $L_p = cT$

$$r_{prms} = \sqrt{\frac{1}{L_p}\int_0^{L_p} r^2 dl} \simeq 0.6239 \cdot 10^{-15} m$$

This value is about 26% smaller than the r_{mean} experimental value.

An other possibility is to compare the r_{prms} toroidal radius with the $r_{phc} \simeq 0.627 \cdot 10^{-15} m$ radius, within which half of the proton charge is contained, and that is shown in figure 2.2. This value, for the proton model, coincides with its r_{prms} radius:

$$r_{phc} = r_{prms}$$

In this case, the above proton radius calculation deviates less than 0.5% from the experimental one 2.2.

6. Proton spin and gyromagnetic factor

6.1. The proposed electromagnetic model based interpretation of proton spin

Analogously to the electron case, the absolute value L_p of the proton's toroidal angular momentum $\boldsymbol{L}_p$ is equal to the reduced Planck constant[5]:

$$L_p = \hbar$$

In the presence of an external magnetic field $\boldsymbol{B}_E$, we can write the vector L_p as the sum of two vectors. One vector is parallel to B_E, and the second one is orthogonal to it:

$$\boldsymbol{L}_p = \boldsymbol{L}_{p\parallel} + \boldsymbol{L}_{p\perp}$$

$$L_{p\parallel} = L_p \cos(\theta)$$

$$L_{p\perp} = L_p \sin(\theta)$$

where θ is the angle between the vectors $\boldsymbol{\mu}_p$ and $\boldsymbol{B}_E$. The proton is therefore subjected to a torque $\boldsymbol{\tau}$:

$$\tau = \left|\boldsymbol{\mu}_p \times \boldsymbol{B}_E\right| = \mu_p B_E \sin(\theta)$$

Consequently, the proton's toroidal structure will be in a Larmor precession, with angular frequency ω_{pP}:

$$\tau = \left|\frac{d\boldsymbol{L}_p}{dt}\right| = L_p \sin(\theta)\frac{d\phi}{dt} = L_p \sin(\theta)\,\omega_{pp}. \tag{6.1}$$

$$\mu_p B_E = \hbar\omega_{pp}$$

What we call "proton spin" s_p is the measured component of its angular momentum vector L_p along the external magnetic field B_E :

$$s_p = \hbar\cos(\theta)$$

Figure 6.1 illustrates the precessing proton structure under an external magnetic field $\boldsymbol{B}_E$.

The measurable angular momentum transitions are also universally quantized to $\hbar$ value. This implies the following for the quantization of the angle θ :

$$\triangle L_{p\parallel} = \pm\hbar \Longrightarrow \theta \in \left\{\frac{\pi}{3}, \frac{2\pi}{3}\right\},\ \cos(\theta) = \pm\frac{1}{2}$$

$$s_p = \pm\frac{\hbar}{2}$$

[5] Under the approach of sections 5.2-5.5, the toroidal angular momentum is $\hbar$ according to the $\boldsymbol{L}_p = \boldsymbol{r}_{pt} \times m_p \boldsymbol{v}_{pt}$ formula, where m_p is the full proton mass. Under the approach of appendix 1, the toroidal angular momentum is $\hbar$ according to the $\boldsymbol{L}_p = \boldsymbol{r}_{pt} \times m_{pt} \boldsymbol{v}_{pt}$ formula, where m_{pt} is the mass component in the toroidal direction that corresponds to the toroidal current loop. See the explanation of appendix 1 about splitting the proton mass into the toroidal and poloidal current loop components.

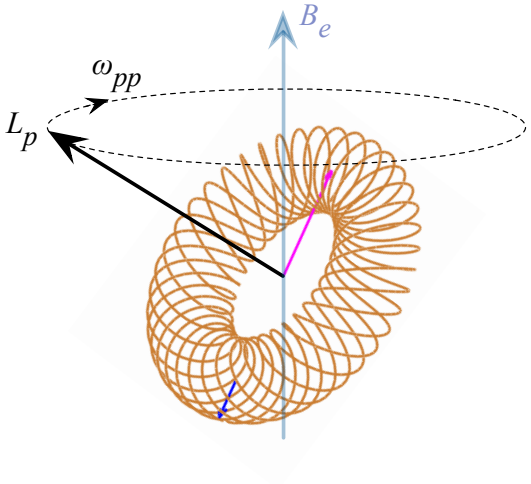

Figure 6.1. The Larmor precessing proton in external magnetic field $\boldsymbol{B}_E$. The proton's toroidal angular momentum vector $\boldsymbol{L}_p$ precesses with angular frequency ω_{pp}.

The two spin values are characterized by two different energy levels, E_L and E_H;

$$\theta = \frac{\pi}{3} \Longrightarrow E_L = -\hbar\omega_{pp}$$

$$\theta = \frac{2\pi}{3} \Longrightarrow E_H = \hbar\omega_{pp}$$

$$\triangle E = E_H - E_L = 2\hbar\omega_{pp}$$

This energy gap $\triangle E$ is equal to $\hbar\omega_{NMRp}$, where ω_{NMRp} is the proton's NMR angular frequency. Therefore:

$$\omega_{NMRp} = 2\omega_{pp} = 2\mu_p B_E = \frac{e}{m_p}\frac{\mu_p}{\mu_N}B_E \tag{6.2}$$

This linear relationship between the applied B_E magnetic field and the resulting $\triangle E$ energy gap is the basis of NMR technology.

The value of ω_{NMRp} can be written as a function of the gyromagnetic factor g_p:

$$\omega_{NMRp} = \frac{e}{2m_p}g_p B_E \tag{6.3}$$

The proton's gyromagnetic-factor g_p is therefore

$$g_p = 2\frac{\mu_p}{\mu_N} = 5.585696018$$

Our calculation precisely matches the CODATA value of the proton's experimentally measured gyromagnetic factor, which is 5.5856946893.

We note that all of the above applies completely analogously to the electron, whose angular momentum value is also $\hbar$. The exact same Larmor precession arises when the electron is placed under an external magnetic field $\boldsymbol{B}_E$, and thus the measured value of its angular momentum becomes $s_e = \pm\frac{\hbar}{2}$ [22]. This phenomenon is the basis of Electron Spin Resonance (ESR) technology: the measured energy gap $\triangle E$ is then equal to $\hbar\omega_{ESR}$, where $\omega_{ESR} = 2\mu_B B_E$ and μ_B is the Bohr magneton.

6.2. The quark model based interpretation of proton spin

When Otto Stern measured the proton's $\mu_p = 2.793\mu_N$ magnetic moment in 1933, most physicists assumed that this measured value is the absolute value of the proton's internal magnetic moment vector. The quark model based magnetic moment calculations were developed under this assumption. With the recent advent of NMR technology, the operators of NMR equipment have recognized that under applied magnetic field the proton is subjected to Larmor precession. However, quark proponents never revised their calculations, which do not consider quarks being in Larmor precession. Any Larmor precession implies that the absolute value of individual quarks' angular momentum vector must be larger than the $\frac{\hbar}{2}$ value assumed in those calculations. Therefore, the quark model based spin interpretation is fundamentally contradicted by the NMR technology.

The Callan-Gross relation, which was mentioned in section 1, implies that a quark's spin is individually measurable, in principle. Yet proton spin measurements always yield $\mu_p = 2.793\mu_N$. One may wonder why the hypothetical quarks' magnetic moments always add up to the same value of $2.793\mu_N$. To explain this constant value, the quark model based proton spin interpretation also requires that the three valence quarks remain in isotropic spin entanglement, which means that their individual spin measurements are always correlated. Specifically, n particles are said to be isotropically spin-correlated, if a measurement made in an *arbitrary* direction θ on *one* of the particles allows us to predict with certainty the spin value of each of the other $n-1$ particles for the same direction θ. Such spin-correlation is required to maintain a constant value of the measured proton magnetic moment. As mentioned in section 1, the color charge hypothesis was introduced to remove the contradiction between the 3-quark spin correlation and the Pauli exclusion principle. However, Paul O'Hara recently proved that Greenberg's postulate does not remove the contradiction with the Pauli exclusion principle: the isotropic spin entanglement of three particles is a mathematical impossibility if their spins are individually measurable. This mathematical contradiction holds regardless of the presence or absence of color charges. Paul O'Hara's proof can be found in the second appendix.

In summary, the quark model based proton spin interpretation involves two fundamental contradictions. Each of these contradictions invalidates the quark model.

7. Conclusions

We have presented a proton model that describes the physical origin of numerous proton parameters, such as its mass, its spin, charge radius, magnetic moment. Despite our model's simplicity, our calculations are in a relatively fair agreement with experimental values. The proton's spherical electric charge generates a Zitterbewegung current over a toroidal surface.

A consistent application of Maxwell's equation thus lead to the discovery of the proposed proton model. The strong similarities with the electron model suggest a universal applicability of fundamental physical laws. Both the electron and the proton comprise an electromagnetic wave, whose formulation can be derived by solving Maxwell's equation. These solutions must not neglect the effects of general relativity, as demonstrated in reference [22] and in our present work. Our proton mass calculation demonstrates that Maxwell's equation remains valid at least down to 10^{-18} m, which is the length scale of the proton's spherical charge radius.

Based on our results, the proton may regain its elementary particle status. The main difference between an electron and a proton is the topology of their Zitterbewegung: a circular Zitterbewegung current in the electron case and a toroidal Zitterbewegung current in the proton case. It remains to be understood why only these two topologies lead to a stable particle.

Acknowledgements

The authors thank Paul O'Hara for insightful discussions of the Pauli exclusion principle, William Stubbs for insightful discussions of high-energy electron-proton scattering data and Giuliano

Bettini for some essential suggestions.

Appendix 1: An alternative approach to the proton geometry calculation[6]

Proton geometry

We calculate the proton radii by applying the toroidal Zitterbewegung model, which was introduced in section 5.1 and is illustrated in figure 5.1.

The total electric energy of the proton is calculated by integrating the energy density of its electric field down to its spherical charge radius:

$$W_e = \frac{e^2}{32\pi^2\epsilon_0}\int_{r_{cp}}^{\infty}\frac{1}{r^4}\cdot 4\pi r^2 dr = \frac{e^2}{8\pi\epsilon_0}\int_{r_{cp}}^{\infty}\frac{1}{r^2}dr = -\frac{e^2}{8\pi\epsilon_0}\,\frac{1}{r}\Big|_{r_{cp}}^{\infty} = \frac{e^2}{8\pi\epsilon_0 r_{cp}}$$

In accordance with Maxwell's equation, the electric an magnetic fields induce each other within the proton. Therefore its electric and magnetic energies must be equal: $W_e = W_m$. From the 938.272 MeV proton mass value we get $W_e = W_m$ =469.136 MeV. We can now calculate the proton's spherical charge radius r_{cp}:

$$r_{cp} = \frac{e^2}{8\pi\epsilon_0 W_e} = 1.5347\cdot 10^{-18}\ \text{m}$$

This calculated r_{cp} value is remarkably similar to the experimental value discussed in section 2.1.

To transform the circular Zitterbewegung model of the positron [22] into a toroidal geometry, the naive approach is to view the positron from rotating reference frame. Such reference frame transformation must take into account the relativistic Thomas precession effect which arises in a rotating reference frame. This effect reduces the apparent lab-frame speed of a circularly orbiting object in proportion to its Lorentz boost factor:

$$\beta_{lab} = \frac{\beta'}{\gamma_{lab}}$$

where $c\beta'$ is the true rotation speed, $c\beta_{lab}$ is the apparent rotation speed in the lab frame, and $\gamma_{lab} = \sqrt{1-\beta_{lab}^2}^{-1}$. When $\beta_{lab} = \frac{1}{\sqrt{2}}$, we get $\beta' = 1$: this limiting value corresponds to the true rotation speed being the speed of light. This result means that in the $\beta_{lab} < \frac{1}{\sqrt{2}}$ regime the toroidal charge distribution is in fact a rotating scaled positron because we can make a rotational change of reference frame which transforms the charge current back to the positron's ring shaped Zitterbewegung. The rotating scaled positron will eventually loose its rotational energy by interacting with other particles, and will thus transform back into an ordinary scaled positron. Therefore, the $\beta_{lab} < \frac{1}{\sqrt{2}}$ regime does not correspond to a stable proton particle. On the other hand, the limiting $\beta_{lab} = \frac{1}{\sqrt{2}}$ value stays invariant under any rotational reference frame transformation, and therefore it corresponds to a truly toroidal charge current, which retains the same geometry in any reference frame. Since the proton retains its basic properties in all reference frames, this $\beta_{lab} = \frac{1}{\sqrt{2}}$ value corresponds to its toroidal Zitterbewegung speed: $v_t = \frac{c}{\sqrt{2}}$.

It follows from Maxwell's equation that electromagnetic waves propagate at the speed of light, which means that the spherical charge moves at a Zitterbewegung speed which is always the speed of light [22]. In the toroidal geometry, the Zitterbewegung speed vector comprises toroidal and poloidal components, which are perpendicular to each other:

$$v_t^2 + v_p^2 = c^2$$

[6] This approach is the perspective of Andras Kovacs

Since we already know the toroidal Zitterbewegung speed, we can calculate the poloidal one as well from he above relationship: $v_p = \frac{c}{\sqrt{2}}$.

The proton's toroidal and poloidal radii
The electron's and positron's circular Zitterbewegung structure is discussed in reference [22]. In order to determine the proton's toroidal and poloidal radii, we must briefly review the positron's magnetic energy and magnetic flux calculation. The positron's canonical momentum, generated by the vector potential A at its spherical charge surface, is $p = eA$. The corresponding positron angular momentum is $\Omega = eAr_{ZBW}$, where r_{ZBW} is the circular Zitterbewegung radius. The electron's and positron's Zitterbewegung radius is experimentally determined by Thomson scattering: $r_{ZBW} = 0.3861592676 \cdot 10^{-12}\ m$. This r_{ZBW} value is referred to in the scientific literature as the reduced Compton radius.

By setting $\Omega = \hbar$, we obtain the norm of the vector potential at the positron's spherical charge surface:

$$A = \frac{\hbar}{er_{ZBW}}.$$

Once we know the vector potential, it is possible to determine the magnetic flux produced by the rotating elementary charge by applying the circulation of the vector potential A:

$$\phi = \oint_{\lambda} A d\lambda = \int_0^{2\pi} \frac{\hbar}{er_{ZBW}} r_{ZBW} d\vartheta = 2\pi\frac{\hbar}{e} = \frac{h}{e} \approx 4.135\,667 \cdot 10^{-15}\ \mathrm{V \cdot s}$$

i.e. the magnetic flux crossing the Zitterbewegung loop is quantized. Now it is possible to calculate the magnetic energy stored in the positron current loop:

$$W_m = \frac{1}{2}\phi I_{positron} = \frac{1}{2} \cdot 2\pi\frac{\hbar}{e} \cdot \frac{ec}{2\pi r_{ZBW}} = \frac{\hbar c}{2r_{ZBW}} \approx 255.5\ \mathrm{keV}$$

which is equal to half the positron rest energy, thereby satisfying the $W_e = W_m$ requirement of an electromagnetic wave. This result demonstrates the correctness of setting the intrinsic angular momentum value to $\hbar$. We note that although the above equation refers to a static current loop, the result stays the same in the case of a circulating elementary charge. To see this, we evaluate the current interaction part of the electromagnetic Lagrangian density:

$$\mathscr{L}_{int} = \boldsymbol{J}_{\triangle} \cdot \boldsymbol{A}_{\triangle} = JA = \frac{I_{positron}}{\pi r_{charge}^2} \cdot \frac{\hbar}{er_{ZBW}} \approx 1.352\,604 \cdot 10^{27}\ \mathrm{J \cdot m^{-3}}$$

By integration over the volume described by the spherical charge trajectory, it is possible to recompute the positron's energy:

$$W_{positron} = \iiint_V JA\, dV = \frac{I_{positron}}{\pi r_{charge}^2} \cdot \frac{\hbar}{er_{ZBW}} \cdot 2\pi^2 r_{ZBW} r_{charge}^2 = \phi I_{positron} \approx 511\ \mathrm{keV}$$

Considering the above expression, we can take the toroidal volume, and divide it into two halves. The spherical positron charge is in one of those halves, and thus the integration volume becomes half of the toroid volume, while the effective current between the integration endpoints is now twice as large. The integration result for $W_{positron}$ remains invariant. By repeating this halving of the toroidal volume segments, we see that the total magnetic energy remains invariant as we approach the circulating spherical charge scenario.

The recognition that the magnetic flux of a Zitterbewegung loop is quantized to $\frac{h}{e}$ is a central result of [22]. We also show that this magnetic flux quantization is equivalent to the electric

charge quantization. Since the proton's charge is the elementary charge e, the $\frac{h}{e}$ magnetic flux quantization must hold true for the proton.

How is the proton's W_m =469.136 MeV magnetic field energy divided between its toroidal and poloidal current loops? The proton's magnetic moment measurement is in fact its toroidal magnetic moment measurement. For an elementary particle, its measured magnetic moment is given by the $\mu = \frac{e\hbar}{2m}$ formula, where the only non-constant factor is the particle mass. Since the proton mass is derived from electromagnetic induction, its excess toroidal magnetic moment is inversely proportional to its toroidal magnetic mass. Therefore the proton's toroidal magnetic energy is:

$$W_{mt} = W_m / \left(\frac{\mu_p}{\mu_N}\right) = \frac{469.136}{2.79285}\ \text{MeV} = 167.978\ \text{MeV}$$

The remaining poloidal magnetic field energy is:

$$W_{mp} = W_m - W_{mt} = 301.158\ \text{MeV}$$

Under the toroidal proton geometry there are two Zitterbewegung loops: a toroidal loop and a poloidal loop. Since both current loops are generated by the elementary charge e, the $\frac{h}{e}$ magnetic flux quantization holds for each current loop. Thus we can calculate the magnetic energy values by applying the $\frac{h}{e}$ magnetic flux quantization condition:

$$W_{mt} = \frac{1}{2}\phi I_{toroidal} = \frac{1}{2}\cdot 2\pi\frac{\hbar}{e}\cdot\frac{ev_t}{2\pi r_{pt}} = \frac{\hbar v_t}{2r_{pt}}$$

$$W_{mp} = \frac{1}{2}\phi I_{poloidal} = \frac{1}{2}\cdot 2\pi\frac{\hbar}{e}\cdot\frac{ev_p}{2\pi r_{pp}} = \frac{\hbar v_p}{2r_{pp}}$$

We thus evaluate the toroidal and poloidal Zitterbewegung radii from the above equations:

$$r_{pt} = \frac{\hbar v_t}{2W_{mt}} = 0.831\ \text{fm}$$

$$r_{pp} = \frac{\hbar v_p}{2W_{mt}} = 0.463\ \text{fm}$$

The obtained 0.831 fm toroidal radius value has a 99% match with the experimentally measured $r_{mean} = 0.839 \pm 0.007$ fm proton charge radius value.

To validate the consistency of our model, we check that the $\mu_p = I_{toroidal}\pi r_{pt}^2$ magnetic moment formula is fulfilled for the toroidal current loop. The above-discussed scaled positron model corresponds to the nuclear magneton:

$$\mu_N = I\pi r_{ZBW}^2 = \frac{ec}{2\pi r_{ZBW}}\pi r_{ZBW}^2 = \frac{ec}{2}r_{ZBW}$$

where $r_{ZBW} = r_{e+}\frac{m_{e+}}{m_p}$=0.2103 fm is the scaled positron's Zitterbewegung radius, while the positron's Zitterbewegung radius and mass values r_{e+}=386.16 fm and m_{e+}=511 keV. We now evaluate the proton's magnetic moment according to the current loop formula:

$$\mu_p = I_{toroidal}\pi r_{pt}^2 = \frac{e\left(c/\sqrt{2}\right)}{2\pi r_{pt}}\pi r_{pt}^2 = \frac{ec}{2\sqrt{2}}r_{pt}$$

$$\mu_p/\mu_N = \left(cr_{pt}/\sqrt{2}\right)/\left(cr_{ZBW}\right) = \frac{1}{\sqrt{2}}\frac{0.831}{0.2103} = 2.794$$

which precisely matches with the experimental μ_p/μ_N ratio. Comparing the above magnetic moment equation with the magnetic energy based r_{pt} calculation, one arrives at the same $\mu_p/\mu_N = r_{pt}/\left(\sqrt{2}r_{ZBW}\right)$ formulation in either case: i.e. these are two ways of expressing the same physics.

The toroidal proton geometry implies that the circulating proton charge is radially distributed between $r_{pt} - r_{pp} - r_{cp}$ and $r_{pt} + r_{pp} + r_{cp}$ distance from its center, i.e. its charge reaches up to 1.296 fm radial distance. This 1.296 fm radius precisely matches the electric polarizability measurements based radius value, that was introduced in section 2.4. Indeed, it is logical to interpret the electric polarizability based radius as the proton charge's furthest distance from its center because one can polarize a charge distribution only within that range where it is physically present.

In summary, we calculated the proton's r_{cp}, r_{pt}, and r_{pp} radii without any parameter fittings, and found that each of them matches well with experimental data.

Appendix 2: Isotropic spin entanglement[7]

By definition, n particles are said to be isotropically spin-correlated (ISC), if a measurement made in an *arbitrary* direction on *one* of the particles allows us to predict with certainty the spin value of each of the other $n-1$ particles for the same direction.

Essentially, to show that ISC states exist only for $n = 2$, it is sufficient to prove that it is impossible to have three such particles. The impossibility of three ISC particles also excludes the possibility of $n \geq 3$ ISC particles.

Suppose that an ISC state exists for $n = 3$. We demonstrate in the following paragraphs that this assumption leads to a mathematical contradiction.

In the interest of clarity, assume without loss of generality that the three ISC particles are such that they are detected to be in $(+,+,+)$ correlation for an arbitrary measurement direction. Later we will generalize the proof to any other correlation type. Define the x axis along this arbitrary direction, and define the z axis in any orthogonal direction to x. We will perform further spin measurements in the $x-z$ plane. Spin measurements in orthogonal directions are statistically independent. Although we know a given particle spin to be $|+\rangle$ along the x axis, a subsequent spin measurement along the z axis of the apparatus gives $\frac{1}{2}$ probability of measuring $|-\rangle$ state. In general, a spin state in direction 2θ with respect to the x axis, given that it is in the state $|+\rangle$ with respect to the x axis, can be constructed from the rotation R and is given by $R|+\rangle = \cos\theta|+\rangle - \sin\theta|-\rangle$. Therefore, in direction 2θ the probability of measuring $|+\rangle$ state is $\cos^2\theta$ and of measuring $|-\rangle$ is $\sin^2\theta$. Taking the $(x, 2\theta)$ direction with respect to two spin correlated particles, the joint probabilities are $P(+,+) = \frac{1}{2}\cos^2\theta$ and $P(+,-) = \frac{1}{2}\sin^2\theta$. Similarly, for the ket $|-\rangle$, $R|-\rangle = \sin\theta|+\rangle + \cos\theta|-\rangle$ and the joint probabilities are $P(-,-) = \frac{1}{2}\cos^2\theta$ and $P(-,+) = \frac{1}{2}\sin^2\theta$. In principle, if three ISC particles exist, a sequence of spin correlated measurements in the directions $2\theta_1$, $2\theta_2$, $2\theta_3$ can be performed on the three entangled particles. Let $(s_1(\theta_1), s_2(\theta_2), s_3(\theta_3))$ represent each particle's observed spin values in the three different directions. Recall that the above stated spin correlation implies that if any particle is measured to be in the $s_i(\theta_i) = |+\rangle$ spin state, the probability of measuring an other particle in the $s_j(\theta_j) = |-\rangle$ spin state becomes $\frac{1}{2}\sin^2(\theta_j - \theta_i)$.

Given that $s_n(\theta_n) = |\pm\rangle$ for each n, there exists only two possible values for each measurement, which we associate with "spin-up" and "spin-down" respectively. Hence, for three measurements there are a total of 8 possibilities. In particular,

$$\{(+,+,-),(+,-,-)\} \subset \{(+,+,-),(+,-,-),(-,+,-),(+,-,+)\}$$

implies the following probability relationship:

[7] This appendix is authored by Paul O'Hara

$$P\{(+,+,-),(+,-,-)\} \leq P\{(+,+,-),(+,-,-),(-,+,-),(+,-,+)\}$$

Consider the meaning of various subsets in the above inequality:

- The $\{(+,+,-),(+,-,-)\}$ subset is interpreted as follows: we measured the spin of particle 1 to be in $|+\rangle$ state and particle 3 to be in $|-\rangle$ state. The corresponding probability is $\frac{1}{2}\sin^2(\theta_3-\theta_1)$.
- The $\{(+,+,-),(-,+,-)\}$ subset is interpreted as follows: we measured the spin of particle 2 to be in $|+\rangle$ state and particle 3 to be in $|-\rangle$ state. The corresponding probability is $\frac{1}{2}\sin^2(\theta_3-\theta_2)$.
- The $\{(+,-,-),(+,-,+)\}$ subset is interpreted as follows: we measured the spin of particle 1 to be in $|+\rangle$ state and particle 2 to be in $|-\rangle$ state. The corresponding probability is $\frac{1}{2}\sin^2(\theta_2-\theta_1)$.

Substituting the above terms into the above inequality, we arrive at

$$\frac{1}{2}\sin^2(\theta_3-\theta_1) \leq \frac{1}{2}\sin^2(\theta_3-\theta_2)+\frac{1}{2}\sin^2(\theta_2-\theta_1)$$

which is Eugene Wigner's interpretation of Bell's inequality. Taking $\theta_3-\theta_2=\theta_2-\theta_1=\frac{\pi}{6}$ and $\theta_3-\theta_1=\frac{\pi}{3}$ gives $\frac{1}{2}\geq\frac{3}{4}$, which is a contradiction. Therefore, three particles cannot all be in the same spin state with probability 1.

Remark: The proof of the above theorem was worked out for $(+,+,+)$ or $(-,-,-)$ type spin correlation. To generalize the proof, suppose that the ISC particles are measured to be $(+,-,+)$ along an arbitrary measurement direction. Then the spin outcomes in the three different directions $\theta_1,\ \theta_2,\ \theta_3$ can be written as:

$$\{(+,-,-),(+,+,-)\} \subset \{(+,-,-),(+,+,-),(-,-,-),(+,+,+)\}$$

Essentially, this means that we flipped the $|+\rangle$ to $|-\rangle$ to represent the state of particle 2. Applying the same probability argument as before, but noting that $P\{(+,-,-),(-,-,-)\}=\frac{1}{2}\cos^2(\theta_3-\theta_2)$, the inequality becomes

$$\frac{1}{2}\sin^2(\theta_3-\theta_1) \leq \frac{1}{2}\cos^2(\theta_3-\theta_2)+\frac{1}{2}\cos^2(\theta_2-\theta_1)$$

Then upon taking $\theta_3-\theta_2=\theta_2-\theta_1=\frac{\pi}{2}-\frac{\pi}{6}$ and $\theta_3-\theta_1=\pi-\frac{\pi}{3}$ gives as before $\frac{1}{2}\geq\frac{3}{4}$, which is a contradiction.

Appendix 3: Physical constants in Natural Units

Conversion constants for natural units:

$1.9732898\cdot10^{-7}\ m\simeq 1eV^{-1}$ length
$6.5821220\cdot10^{-16}\ s\simeq 1eV^{-1}$ time
$2.99792458\cdot10^{8}\ ms^{-1}=1$ speed
$1.5192669\cdot10^{15}\ Hz\simeq 1eV$ frequency
$8.1193997\cdot10^{-13}\ N\simeq 1eV^{2}$ force
$1.8755460\cdot10^{-18}\ C=1$ charge

Relevant physical constants in natural units:

$h = 2\pi$ Planck's constant $\left(6.62607015 \cdot 10^{-34} JHz^{-1}\right)$
$\hbar = {}^{h}/_{2\pi} = 1$ reduced Planck's constant
$\varepsilon_0 = \frac{1}{4\pi}$ vacuum permittivity
$\mu_0 = 4\pi$ vacuum magnetic permeability
$c = 1$ light speed in vacuum $\left(2.99792458 \cdot 10^{8} ms^{-1}\right)$
$\alpha^{-1} \simeq 137.036$ inverse of the fine structure constant
$e = \pm\sqrt{\alpha} \simeq 0.085424546$ $\left(1.602176634 \cdot 10^{-19} C\right)$ elementary charge
$\mu_N \simeq 4.552225759 \cdot 10^{-11}\, eV^{-1}$ $\left(5.0507837461 \cdot 10^{-27} JT^{-1}\right)$ nuclear magneton
$\mu_{pC} \simeq 1.271367397 \cdot 10^{-10}\, eV^{-1}$ $\left(1.41060679736 \cdot 10^{-26} JT^{-1}\right)$ proton magnetic moment
$\frac{\mu_p}{\mu_N} \simeq 2.79284734463$ CODATA proton magnetic moment to nuclear magneton ratio
$m_p \simeq 0.93827208816 \cdot 10^{9}\, eV$ proton mass
$\lambda_p \simeq 6.696549362 \cdot 10^{-9}\, eV^{-1}$ $\left(1.32140985539 \cdot 10^{-15} m\right)$ proton Compton wavelength
$A_e \simeq 5.981875085 \cdot 10^{6} eV$ norm of the vector potential of the electron charge
$V_e = A_e$ electric potential at surface of the electron's charge
$\Phi_M = \frac{\hbar}{e} = 2\pi\alpha^{-1/2} \simeq 73.55246020$ elementary charge's magnetic flux
$m_e = \omega_e \simeq 0.51099895 \cdot 10^{6} eV$ electron rest mass
$\omega_e = m_e$ electron's charge angular speed
$T_e = \frac{2\pi}{\omega_e}$ electron Zitterbewegung period
$r_e = \omega_e^{-1} \simeq 1.956951198 \cdot 10^{-6} eV^{-1}$ $\left(0.3861592676 \cdot 10^{-12} m\right)$ electron radius
$r_{ce} = \alpha r_e$ electron charge radius
$R_{p,exp} \simeq 4.264 \cdot 10^{-9}\, eV^{-1}$ $\left(0.8414 \cdot 10^{-15} m\right)$ "proton charge radius" CODATA value

Appendix 4: Proton model parameters

parameter set 1 (section 5):

$r_{pp} = m_p^{-1} = \frac{\lambda_p}{2\pi} \simeq 1.06578893 \cdot 10^{-9}\, eV^{-1}$ $\left(0.2103089103 \cdot 10^{-15} m\right)$ proton torus minor radius
$r_{pt} = \eta r_{pp} \simeq 2.976586476 \cdot 10^{-9}\, eV^{-1}$ $\left(0.5873608214 \cdot 10^{-15} m\right)$ proton torus major (toroidal) radius
$r_{cp} = \alpha r_{pp} \simeq 7.777437549 \cdot 10^{-12}\, eV^{-1}$ $\left(1.534698267 \cdot 10^{-18} m\right)$ proton spherical charge radius
$r_{prms} \simeq 3.16 \cdot 10^{-9}\, eV^{-1}$ $\left(0.624 \cdot 10^{-15} m\right)$ proton charge Root Mean Square radius
$r_{phc} = r_{prms}$ radius that contains half of the proton charge
$\eta = \frac{r_{pt}}{r_{pp}} = \sqrt{\frac{39}{5}} \simeq 2.792848009$ proton torus aspect ratio
$v_{pt} = \eta^{-1} c$ toroidal component of the charge speed c
$A_p = \frac{m_p}{e} \simeq 1.098363601 \cdot 10^{10}\, eV$ the absolute value of the vector potential at the proton charge
A_{pt} toroidal component of the vector potential A_p
$L_p = eA_{pt} r_{pt} = \hbar = 1$ the proton's toroidal angular momentum
$eA_{pt} r_{pt} \cos(\vartheta) = \pm 1/2\hbar$ $(\vartheta \in \{\pi/3, 2\pi/3\})$ measured proton spin
$\mu_p = \frac{r_{pt}}{2} e \simeq 2.792848009\, \mu_N$ proton model magnetic moment
$\Phi_p = \frac{\hbar}{e} \simeq 73.55246020$ proton model magnetic flux quantum

parameter set 2 (appendix 1):

$r_{pp} \simeq 2.3465 \cdot 10^{-9}\, eV^{-1}$ $\left(0.463 \cdot 10^{-15} m\right)$ proton torus minor (poloidal) radius
$r_{pt} \simeq 4.2113 \cdot 10^{-9}\, eV^{-1}$ $\left(0.831 \cdot 10^{-15} m\right)$ proton torus major (toroidal) radius
$r_{cp} \simeq 7.777437549 \cdot 10^{-12}\, eV^{-1}$ $\left(1.534698267 \cdot 10^{-18} m\right)$ proton spherical charge radius
$v_{pt} = \frac{c}{\sqrt{2}}$ toroidal component of the charge speed c
$L_p = \hbar = 1$ the proton's toroidal angular momentum
$\hbar \cos(\vartheta) = \pm 1/2\hbar$ $(\vartheta \in \{\pi/3, 2\pi/3\})$ measured proton spin
$\mu_p \simeq 2.792848009\, \mu_N$ proton model magnetic moment
$\Phi_p = \frac{\hbar}{e} \simeq 73.55246020$ proton model magnetic flux quantum

References

[1] P. Anastasovski, T. Bearden, C. Ciubotariu, W. Coffey, L. Crowell, G. Evans, M. Evans, R. Flower, S. Jeffers, A. Labounsky, B. Lehnert, M. Mészáros, P. Molnar, and S. Roy, *Aharonov-bohm effect as the basis of electromagnetic energy inherent in the vacuum*, Foundations of Physics Letters, 15 (2002), pp. 561–568.
[2] D. Bergman, *The real proton*, Foundations of Science, 3 (2000).
[3] G. Bettini, *Clifford Algebra, 3 and 4-Dimensional Analytic Functions with Applications. Manuscripts of the Last Century.*, viXra.org, Quantum Physics (2011), pp. 1–63. http://vixra.org/abs/1107.0060.
[4] A. Beyer, *The rydberg constant and proton size from atomic hydrogen*, Science, 358 (2017).
[5] N. Bezginov, *A measurement of the atomic hydrogen lamb shift and the proton charge radius*, Science, 365 (2019).
[6] J. D. Bjorken, *Inelastic electron-proton and gamma-proton scattering and the structure of the nucleon*, Physical Review, 185 (1969).
[7] O. Chamberlain, *Example of an antiproton-nucleon annihilation*, Physical Review, 102 (1956).
[8] T. D. N. S. A. Committee, *The frontiers of nuclear science - a long range plan*, (2007).
[9] P. Cote and M. Johnson, *Groupthink and the blunder of the gauges*, arXiv, (2011).
[10] Z. F. Cui, *Fresh extraction of the proton charge radius from electron scattering*, Physical Review Letters, 127 (2021).
[11] A. Di Tommaso and G. Vassallo, *Electron structure, Ultra-Dense Hydrogen and Low Energy Nuclear Reactions*, Journal of Condensed Matter Nuclear Science, 29 (2019), pp. 525–547.
[12] H. Fonvieille, *Virtual compton scattering and nucleon generalized polarizabilities*, Progress in Particle and Nuclear Physics, 113 (2020).
[13] M. Gell-Mann, *A schematic model of baryons and mesons*, Physics Letters, 8 (1964).
[14] K. Griffioen, C. Carlson, and S. Maddox, *Consistency of electron scattering data with a small proton radius*, Physical Review C, 93 (2016).
[15] A. Grinin, *Two-photon frequency comb spectroscopy of atomic hydrogen*, Science, 370 (2020).
[16] F. Halzen, *Quarks and leptons: An introductory course in modern particle physics*, John Wiley and Sons, (1984).
[17] L. N. Hand, *Electric and magnetic form factors of the nucleons*, Reviews of Modern Physics, 35 (1963).
[18] L. Hively and G. Giakos, *Toward a more complete electrodynamic theory*, International Journal of Signal and Imaging Systems Engineering, 5 (2012), pp. 3–10.
[19] L. Hively and A. Loebl, *Classical and extended electrodynamics*, Physics Essays, 32 (2019), pp. 112–126.
[20] R. L. Jaffe, *Where does the proton really get its spin?*, Physics Today, (1995).
[21] O. Keller and L. Hively, *Ohmura's extended electrodynamics: longitudinal aspects in general relativity*, Journal of Physics Communications, 3 (2019), p. 115002.
[22] A. Kovacs, G. Vassallo, P. O'Hara, F. Celani, and A. Di Tommaso, *Unified Field Theory and Occam's Razor*, World Scientific, 04 2022.
[23] A. Kovacs, V. Zatelepin, and D. Baranov, *Signatures of 1.5 MeV leptons in nuclear reactions*, Journal of Physics - Conference Series, (2023).
[24] S. E. Kuhn, *Nucleon structure functions: Experiments and models*, Proceedings of the 12th Annual HUGS at CEBAF, 231 (1998).
[25] J. Kuti, *Inelastic lepton-nucleon scattering and lepton pair production in the relativistic quark-parton model*, Physical Review D, 4 (1971).
[26] R. Li, *Measured proton electromagnetic structure deviates from theoretical predictions*, Nature, 611 (2022).
[27] Y. H. Lin, *New insights into the nucleon's electromagnetic structure*, Physical Review Letters, 128 (2022).
[28] A. I. L'vov and V. A. Petrun'kin, *Dispersion theory of proton compton scattering in the first and second resonance regions*, Physical Review C, 55 (1997).
[29] R. L. Mills, J. J. Farrell, and W. R. Good, *Unification of Spacetime, the Forces, Matter, and Energy*, Science Press, Ephrata, PA 17522, 1992.
[30] G. Modanese, *Generalized maxwell equations and charge conservation censorship*, Modern Physics Letters B, 31 (2016).
[31] ——, *Unified Field Mechanics II: Formulations and Empirical Tests - Covariant Formulation of Aharonov-Bohm Electrodynamics and Its Application to Coherent Tunneling*, 2018.
[32] E. Perez, *The quark and gluon structure of the proton*, Reports on Progress in Physics, 76 (2013).
[33] D. Reed, *Unravelling the potentials puzzle and corresponding case for the scalar longitudinal electrodynamic wave*, Journal of Physics: Conference Series, 1251 (2019).
[34] D. Reed and L. Hively, *Implications of gauge-free extended electrodynamics*, Symmetry, 12 (2020).
[35] H. Reiss, *Fundamental formulation of light-matter interactions revisited*, Physical Review A, 100 (2019).
[36] G. Rousseaux, *The gauge non-invariance of classical electromagnetism*, Annales de la Fondation Louis de

Broglie, 30 (2005).
[37] W. L. Stubbs, *The nucleus of atoms: One interpretation*, CreateSpace Independent Publishing Platform, (2018).
[38] V. Tvaskis, *Proton and deuteron f2 structure function at low q2*, Physical Review C, 81 (2010).
[39] K. J. van Vlaenderen, *A generalisation of classical electrodynamics for the prediction of scalar field effects*, arXiv, (2003).
[40] C. S. Wood, *Measurement of parity nonconservation and an anapole moment in cesium*, Science, 275 (1997).
[41] D. A. Woodside, *Three-vector and scalar field identities and uniqueness theorems in euclidean and minkowski spaces*, American Journal of Physics, 77 (2009), pp. 438–446.
[42] W. Xiong, *A high precision measurement of the proton charge radius at jlab*, PhD dissertation, Duke University, (2020).